IOP Publishing Phys. Med. Biol. 65 (2020) 025004 (12pp) https://doi.org/10.1088/1361-6560/ab5fee

Physics in Medicine & Biology

IPEM Institute of Physics and Engineering in Medicine

PAPER

RECEIVED
22 October 2019

REVISED
25 November 2019

ACCEPTED FOR PUBLICATION
9 December 2019

PUBLISHED
16 January 2020

Nuclear-interaction correction for patient dose calculations in treatment planning of helium-, carbon-, oxygen-, and neon-ion beams

Taku Inaniwa[1], Sung Hyun Lee, Kota Mizushima, Dousatsu Sakata, Yoshiyuki Iwata, Nobuyuki Kanematsu and Toshiyuki Shirai

Department of Accelerator and Medical Physics, National Institute of Radiological Sciences, QST, 4-9-1 Anagawa, Inage-ku, Chiba 263-8555, Japan

[1] Author to whom any correspondence should be addressed.

E-mail: inaniwa.taku@qst.go.jp

Keywords: heavy-ion radiotherapy, inelastic nuclear interactions, dose calculation

Abstract

In charged-particle therapy treatment planning, the patient is conventionally modeled as variable-density water, i.e. stopping effective density ρ_S, and the planar integrated dose distribution measured in water (PID) is applied for patient dose calculation based on path length scaling with the ρ_S. This approximation assures the range accuracy of charged-particle beams. However, it causes dose calculation errors due to water nonequivalence of body tissues in nuclear interactions originating from compositional differences. We had previously proposed and validated a PID correction method for the errors in carbon-ion radiotherapy. In the present study, we verify the PID correction method for helium-, oxygen-, and neon-ion beams. The one-to-one relationships between ρ_S and the nuclear effective density ρ_N of body tissues were constructed for helium-, carbon-, oxygen-, and neon-ion beams, and were used to correct the PIDs to account for the dose calculation errors in patient. The correction method was tested for non-water materials with un-scanned and scanned ion beams. In un-scanned beams penetrating the materials, the dose calculation errors of up to 5.9% were observed at the Bragg peak region, while they were reduced to $\leqslant$0.9% by the PID correction method. In scanned beams penetrating olive oil, the dose calculation errors of up to 2.7% averaged over the spread-out Bragg peak were observed, while they were reduced to $\leqslant$0.4% by the correction method. To investigate the influence of water nonequivalence of body tissues on tumor dose, we carried out a treatment planning study for prostate and uterine cases. The tumor over-doses of 0.9%, 1.8%, 2.0%, and 2.2% were observed in the uterine case for the helium-, carbon-, oxygen-, and neon-ion beams, respectively. These dose errors could be diminished by the PID correction method. The present results verify that the PID correction method is simple, practical, and accurate for treatment planning of these four ion species.

1. Introduction

Charged-particle therapy with protons and carbon ions offers a more localized dose distribution to a tumor than conventional radiotherapy due to their intrinsic properties such as an advantageous depth dose profile (Tobias *et al* 1971), a small lateral scattering (Gottschalk 2010), and an increasing relative biological effectiveness (RBE) toward the Bragg peak (Blakely *et al* 1979). These properties of the ion beams, however, have resulted in the need for more accurate patient dose calculations in treatment planning. The analytical dose calculation of charged-particle therapy is conventionally based on the planar integrated dose distribution measured in water (PID) with patient heterogeneity correction by path length scaling with the effective depth. The effective depth for charged-particle beams is a linear integration of stopping effective density ρ_S, which is defined as the stopping power ratio of the body tissues to that of water, along the beam path. Therefore, in treatment planning, x-ray computed tomography (CT) images of patients represented in Hounsfield units (HU) are converted into a ρ_S distribution

using a predetermined calibration table (Schneider *et al* 1996, Kanematsu *et al* 2003, 2016). These procedures focus on the range accuracy, but possibly cause dose calculation errors due to water nonequivalence of body tissues in nuclear interactions originating from compositional differences. The dosimetric effect in a patient was estimated to be less than 1% for proton radiotherapy (Inaniwa *et al* 2016), while the effect would amount to 3% or more for extreme clinical cases in carbon-ion radiotherapy (Inaniwa *et al* 2015c). To account for the dosimetric effect, Kanematsu *et al* (2012) formulated a semi-empirical relation between ρ_S and nuclear effective density ρ_N, which is defined as the ratio of the probability of nuclear interactions of ions in body tissues to that in water. Inaniwa *et al* (2015a) proposed a correction method for PID using the relationship between ρ_S and ρ_N of body tissues for scanned carbon-ion beams. The PID correction method was validated and has been routinely used in treatment planning of scanned carbon-ion radiotherapy at the National Institute of Radiological Sciences (NIRS).

Currently, several groups are investigating the potential of helium- (Krämer *et al* 2016, Tessonnier *et al* 2017a, 2017b), oxygen- (Kurz *et al* 2012, Sokol *et al* 2017), or neon-ion beams (Inaniwa and Kanematsu 2018) besides proton and carbon-ion beams to effectively treat tumors with different radiation sensitivities. In addition, the beam delivery of multiple ion species in a single treatment session has been investigated to maximize the therapeutic effects of charged-particle beams (Böhlen *et al* 2012, 2013, Krämer *et al* 2014, Inaniwa *et al* 2017, Kopp *et al* 2020). The inelastic nuclear interaction cross sections of helium, oxygen, and neon ions in materials are different from the cross sections of protons or carbon ions (Sihver *et al* 1993). The dosimetric effects of water nonequivalence of body tissues may be larger for heavier ions due to the increased probability of inelastic nuclear interactions (Schneider *et al* 2002, Palmans and Verhaegen 2005). Therefore, it is essential to correct the dosimetric effects especially for oxygen- and neon-ion beams.

In this study, we reformulated the ρ_S-to-ρ_N relationships for helium-, carbon-, oxygen-, and neon-ion beams using the standard elemental composition data of body tissues. The PID correction method developed for scanned carbon-ion beams (Inaniwa *et al* 2015a) was extended for helium-, oxygen-, and neon-ion beams. The correction method is integrated into the in-house treatment planning software (Inaniwa *et al* 2014, 2015a, 2015b, Inaniwa and Kanematsu 2015) for scanned charged-particle therapy. We evaluated its accuracy in clinical use through experiments using the four ion beams with various materials.

2. Materials and methods

2.1. ρ_S-to-ρ_N relationship for body tissues

2.1.1. Body tissues

We use 92 of the International Commission of Radiation Units (ICRU) body tissues (ICRU 1992) excluding obsolete, extreme, or artificially extracted materials such as ICRU-33 soft tissue, hydroxyapatite, calcifications, lipid, carbohydrate, cell nucleus, cholesterol, protein, and urinary stones, as in our previous studies (Kanematsu *et al* 2012, Inaniwa *et al* 2015a, 2016). The elemental composition and elemental mass fraction of the body tissues are compiled in the ICRU report.

2.1.2. Stopping effective density ρ_S

The Bethe formula is used to calculate the stopping effective density ρ_S of a body tissue material,

$$\rho_S = \rho_e \left(\ln \frac{2m_e c^2 \beta^2}{I(1-\beta^2)} - \beta^2 \right) \Big/ \left(\ln \frac{2m_e c^2 \beta^2}{I_w(1-\beta^2)} - \beta^2 \right), \tag{1}$$

where ρ_e is the electron density of the material relative to water, $m_e = 0.511$ MeV/c^2 is the electron mass, c is the speed of light, β is the speed of the projectile scaled by c, and I and I_w are the mean excitation energies of the material and water. The ρ_e and the I-value of body tissues are determined by equations (3) and (4) described in Inaniwa *et al* (2015a) with the elemental composition data compiled in the ICRU report. We used the effective β of 0.43 in ρ_S estimation to minimize the range errors (Inaniwa and Kanematsu 2016).

2.1.3. Nuclear effective density ρ_N

Under an assumption that the energy dependence of the nuclear interaction probability of projectiles in body tissues and in water is the same in the therapeutic energy range, the nuclear effective density ρ_N of a body tissue material is given by

$$\rho_N = \rho_m \left(\sum_i w_i \frac{\sigma_{Ni}}{A_{ri}} \right) \Big/ \left(\frac{2\sigma_{NH} + \sigma_{NO}}{M_{rw}} \right). \tag{2}$$

(Kanematsu *et al* 2012, Inaniwa *et al* 2015a), where ρ_m is the mass density of the material relative to water, and w_i and A_{ri} are the elemental mass fraction and the atomic weight of element i. σ_{Ni} is the geometrical cross section for

collision between a projectile nucleus of mass number A and a target nucleus of mass number A_{ri} calculated by Sihver's formula (Sihver *et al* 1993, Sihver and Mancusi 2009). σ_{NH} and σ_{NO} are the cross sections of hydrogen and oxygen nuclei and $M_{rw} = 18.015$ is the molecular weight of water.

2.1.4. ρ_S-to-ρ_N relationship

We calculated ρ_S and ρ_N of the selected 92 ICRU body tissues, and formulated polyline conversion functions between them for helium-, carbon-, oxygen-, and neon-ion beams.

2.2. Correction method

2.2.1. Attenuation correction factor

Inelastic nuclear interactions lead to an attenuation of projectile fluence with increasing penetration depth. If the patient's body is treated as water of inhomogeneous density, the projectile fluence at a depth z along the beam path can be approximated as

$$\Phi_w(z) = \Phi_0 \exp(-s_S(z)/\lambda), \tag{3}$$

where Φ_0 is the projectile fluence at the patient surface, λ is the mean-free path of projectiles in water, and s_S is the stopping effective depth defined by

$$s_S(z) = \int_0^z \rho_S(z')\,dz'. \tag{4}$$

Due to the water-nonequivalence of body tissues in nuclear interactions, the actual projectile fluence at the depth z in the patient would be

$$\Phi_p(z) = \Phi_0 \exp(-s_N(z)/\lambda), \tag{5}$$

where s_N is the nuclear effective depth defined by

$$s_N(z) = \int_0^z \rho_N(z')\,dz'. \tag{6}$$

The attenuation correction factor ϕ_w^p at the depth z, defined as the ratio of the attenuation of projectiles in the patient to that in water, is then given by

$$\phi_w^p(z) = \Phi_p(z)/\Phi_w(z) = \exp[(s_S(z) - s_N(z))/\lambda]. \tag{7}$$

For the mean free path λ, we used 625.4, 256.0, 215.7, and 190.1 mm for helium-, carbon-, oxygen-, and neon-ion beams, respectively, which were determined by Geant4-based Monte Carlo simulations (Agostinelli *et al* 2003).

2.2.2. PID correction

In scanned charged-particle therapy, the Bragg peak of a narrow pencil beam is delivered to positions referred to as 'spots' across the target volume. The dose distribution in a patient is formed by superposing the dose distributions of the pencil beam delivered to the spots with varying spot weights. In analytical dose calculations, we modeled the dose distribution of scanned ion beams as the superposition of three components (Inaniwa *et al* 2014, Inaniwa and Kanematsu 2015). For the calculations of carbon-, oxygen-, and neon-ion beams, we assumed the first, second, and third components were composed of primary ions, heavy fragments with atomic number $Z \geqslant 3$, and light fragments with $Z \leqslant 2$. For helium-ion beam calculations, we assumed both the second and third components were composed of fragments with $Z = 1$ with different transverse spreads. The dose distribution of the pencil beam at the jth spot (jth beamlet) with initial energy E_{0j} is then described as

$$d_j(x,y,z) = \sum_{n=1}^{3} d_{n,j}(x,y,z) = \sum_{n=1}^{3} \left[P_n\left(s_S(z), E_{0j}\right) \cdot G\left(x,y,\sigma_{n,j}(z)\right)\right], \tag{8}$$

where x- and y-coordinates are in the lateral orthogonal directions, and the z-coordinate is in the direction of the beam axis. $d_{n,j}$ is the dose contribution from the nth component to d_j, while $P_n\left(s_S, E_{0j}\right)$ is the planar integration of $d_{n,j}$ over the infinite x-y plane at a stopping effective depth s_S. $G(x,y,\sigma)$ is the two-dimensional axially symmetric Gaussian function with the standard deviation σ in the transverse direction. $\sigma_{n,j}(z)$ is the σ of the nth component of the jth beamlet at z. The parameters describing d_j were determined from the PID and beam profile measurements in water combined with the Monte Carlo simulation (Inaniwa *et al* 2014).

The number of primary particles decreases with depth via inelastic nuclear interactions. The number of fragment particles will inversely increase with the reduction in the number of primary particles. Following Inaniwa *et al* (2015a), we assumed that the first and third dose components would be modified by factors ϕ_w^p while the second dose component would be unaffected by water nonequivalence, as

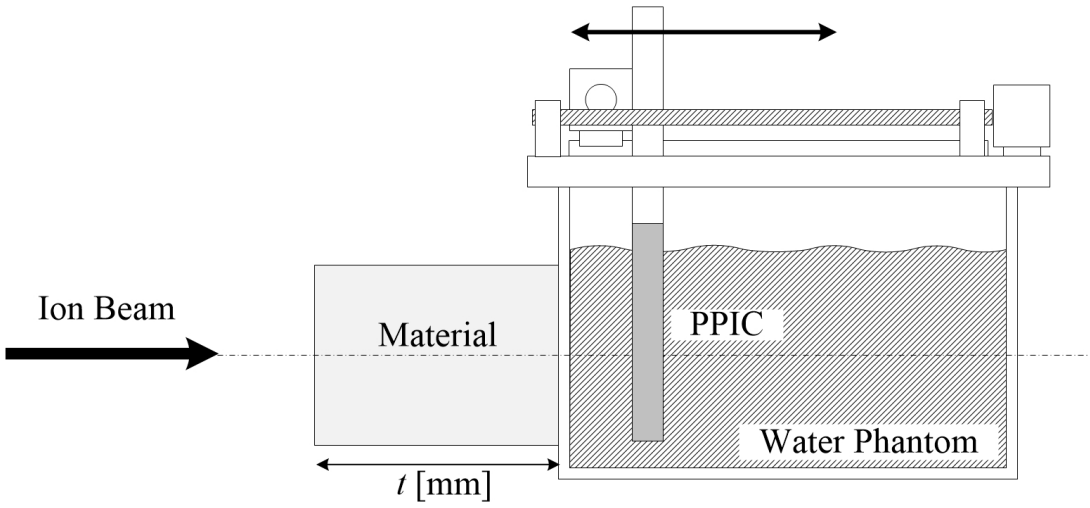

Figure 1. Side view of the apparatus for un-scanned and scanned beam experiments. PPIC = plane-parallel ionization chamber.

Table 1. List of materials and their stopping effective density ρ_S and nuclear effective density ρ_N for helium-, carbon-, oxygen-, and neon-ion beams.

Material	ρ_S	$\rho_N(^4He)$	$\rho_N(^{12}C)$	$\rho_N(^{16}O)$	$\rho_N(^{20}Ne)$
water	1.000	1.000	1.000	1.000	1.000
Ethanol	0.818	0.864	0.877	0.880	0.883
40% K_2HPO_4	1.310	1.241	1.195	1.182	1.172
Olive oil	0.935	1.014	1.021	1.023	1.025
Milk	1.039	1.054	1.047	1.045	1.043

$$d'_j(x,y,z) = \sum_{n=1}^{3} d'_{n,j}(x,y,z) = \phi_w^p P_{1,j} G_{1,j} + P_{2,j} G_{2,j} + \frac{1}{\phi_w^p} P_{3,j} G_{3,j}, \tag{9}$$

where $P_{n,j}$ and $G_{n,j}$ are the abbreviations of $P_n\left(s_S(z), E_{0,j}\right)$ and $G\left(x, y, \sigma_{n,j}(z)\right)$, respectively. The PID of the corrected distribution is obtained by

$$P'_j(z) = \iint d'_j(x,y,z)\,dxdy = \phi_w^p P_{1,j} + P_{2,j} + \frac{1}{\phi_w^p} P_{3,j}. \tag{10}$$

2.3. Experimental validation

The dosimetric influence of the water nonequivalence of the materials as well as the accuracy of the PID correction method was confirmed through irradiation experiments with un-scanned and scanned ion beams.

2.3.1. Un-scanned beams

We conducted experiments with un-scanned helium-, carbon-, oxygen-, and neon-ion beams of E/A = 166.0, 313.2, 373.9, and 430.0 MeV, respectively, extracted from the Heavy Ion Medical Accelerator in Chiba (HIMAC) of the NIRS. The transverse width of the beams was narrowed to 5–10 mm full width at half maximum (FWHM), and their longitudinal width, i.e. their Bragg peak width, was expanded by a ripple filter for Gaussian range modulation of 1.0 mm (rms). The experimental setup is shown in figure 1. At first, the PIDs of the four ion beams in water without the materials were measured as references. Then, the materials listed in table 1 were placed in front of the water phantom to measure the PID behind the materials. All materials were in the liquid phase and were put into a container of 100 × 100 × 100 mm^3 with polymethyl methacrylate (PMMA) walls of 1 mm thickness. The PIDs at varied depth z in water were measured with the plane-parallel ionization chamber (PPIC) with a sensitive area of 15 cm in diameter. The size of the sensitive area allows the detection of large-angle scattered particles.

ρ_S values of the biological materials, i.e. olive oil and milk, were derived from measured CT images using a CT Hounsfield units (HU)-to-ρ_S conversion table constructed for one of the CT scanners at the NIRS based on the method described by Kanematsu *et al* (2016). ρ_N values of the biological materials were then obtained from the established polyline conversion functions between ρ_S and ρ_N described in 2.1. ρ_S values of the tissue substitute

materials, i.e. water solution of 40% potassium phosphate (40% K_2HPO_4) and ethanol, were derived from the measured shifts of Bragg-peak depths Δt behind the materials from those behind water as

$$\rho_S = 1 + \Delta t/t, \tag{11}$$

where $t = 100$ mm is the thickness of the materials. ρ_N values of the tissue substitute materials were then calculated according to equation (2) with the measured ρ_S, the elemental composition, and the elemental I-values of the substitute.

The attenuation correction factor ϕ_w^p at the depth z in the materials was calculated by equation (7) with the ρ_S and ρ_N in equations (4) and (6). The dose distributions behind the materials and their PIDs were then calculated with equations (9) and (10), respectively.

We compared the measured PID behind the materials to the corrected and uncorrected PIDs. The PIDs were plotted as a function of the distance from R_{90} at which the PID decreased to 90% of its maximum, $l \equiv z - R_{90}$, and were divided into three regions, the proximal region for $l \leqslant -10$ mm, the peak region for $-10 < l \leqslant 0$ mm, and the tail region for $5 \leqslant l$ mm, respectively. To quantify the dosimetric effect of the water nonequivalence in each region, we introduced scaling factors ξ_c and ξ_{uc} with respect to the corrected and uncorrected PIDs, respectively. The factors ξ_c and ξ_{uc} were derived from fitting to the measured PIDs behind the non-water materials.

2.3.2. *Scanned beams*

The olive oil in the container was positioned in front of the water phantom (figure 1). A target volume of $80 \times 80 \times 40\,\text{mm}^3$ was defined in the water phantom. The physical dose of 1 Gy was prescribed to the target with scanned helium-, carbon-, oxygen-, and neon-ion beams. The spots were arranged on regular grids of 2 mm spacing, which covered the target volume with adequate margins for lateral and distal falloffs. The number of ions delivered to each spot was determined by the optimization algorithm of the treatment planning software (Inaniwa *et al* 2014, Inaniwa and Kanematsu 2015) in conjunction with the extended PID correction. The central-axis doses at varied depth z in the water phantom were measured by a Markus ionization chamber (PTW Type 34045). To verify the accuracy of the extended PID correction in treatment planning, we compared the measured and planned (corrected) dose distributions for the four ion beams. In addition, to quantify the influence of water nonequivalence of the olive oil on dose, we compared the measured and recalculated (uncorrected) dose distributions without the correction for the beams.

2.4. Case study

To investigate the effect of water nonequivalence of tissues in nuclear interactions on tumor dose, we made a treatment planning case study with scanned helium-, carbon-, oxygen-, and neon-ion beams. We took prostate and uterine cases treated at the NIRS with carbon-ion beams. For both cases, we used real planning CT images, in which clinical target volumes had been delineated by radiation oncologists. CT data of the patients represented in HU were converted to the ρ_S distribution using a predetermined HU-to-ρ_S conversion table. The ρ_S distribution of the patients were then converted to ρ_N distributions of the respective beams for patient dose calculations with the nuclear interaction correction to derive the corrected dose distributions. In the treatment-planning, we followed one of several beams configured in the original treatments. The planned (corrected) dose distributions D_c were then recalculated without the nuclear interaction correction to derive the uncorrected dose distributions D_{uc}. The corrected and uncorrected dose distributions were compared with each other.

For the prostate cancer case, in which a part of the therapeutic ion beams passes through the bony pelvis, we made single-field uniform dose (SFUD) plans with lateral beams of respective ions. The clinical dose of $D_{pre} = 4.30$ Gy (RBE) in the RBE definition at the NIRS (Inaniwa *et al* 2015b) was prescribed to the target.

For the uterine case, in which a part of the therapeutic beams passes through the thick subcutaneous and visceral fat layers, we made SFUD plans with anterior beams of respective ions. The clinical dose of $D_{pre} = 4.80$ Gy (RBE) was prescribed to the target.

3. Results

3.1. ρ_S-to-ρ_N relationships of body tissues

Figure 2 shows relationships between ρ_S and ρ_N of the standard body tissues for helium-, carbon-, oxygen-, and neon-ion beams. The fitting polyline functions with the vertices summarized in table 2 generally reproduced the ρ_S-to-ρ_N relationships of the tissues. In the adipose tissue region with $0.9 \lesssim \rho_S \lesssim 1.0$, ρ_N was higher than ρ_S. Contrarily, in the bone tissue region with $\rho_S \gtrsim 1.05$, ρ_N was lower than ρ_S and the discrepancy between them increased with ρ_S. The discrepancy between ρ_N and ρ_S in the bone tissue region was larger for heavier ions. For the materials with $\rho_S > 1.884$ ($\rho_e > 2.00$), where there were no standard body tissues, we assumed $\rho_N = \rho_S$ to avoid false corrections for non-biological materials.

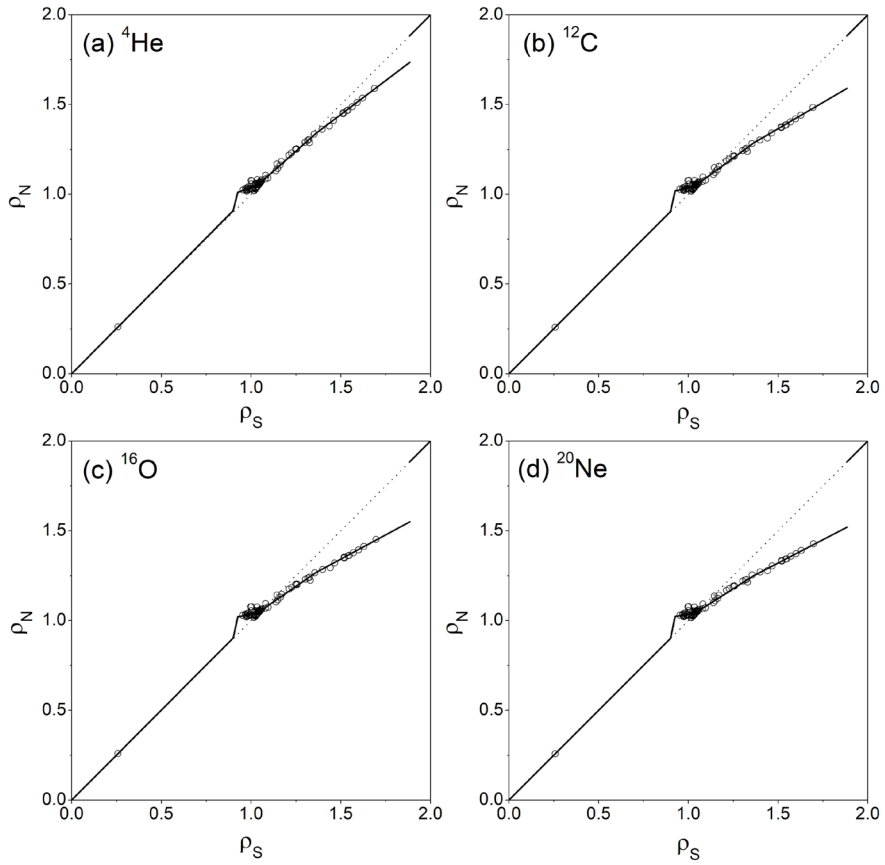

Figure 2. Relationships between stopping effective density ρ_S and nuclear effective density ρ_N of the standard body tissues for (a) helium-, (b) carbon-, (c) oxygen-, and (d) neon-ion beams. Open circles are the values for the ICRU body tissues, solid polylines are the ρ_S-to-ρ_N conversion functions, and dotted lines are the function $\rho_N = \rho_S$ for the uncorrected dose calculation.

Table 2. Vertices of the polyline conversion functions from stopping effective density ρ_S to nuclear effective density ρ_N for helium-, carbon-, oxygen-, and neon-ion beams.

ρ_S	$\rho_N(^4\mathrm{He})$	$\rho_N(^{12}\mathrm{C})$	$\rho_N(^{16}\mathrm{O})$	$\rho_N(^{20}\mathrm{Ne})$
0	0	0	0	0
0.900	0.910	0.904	0.903	0.901
0.925	1.011	1.019	1.021	1.023
1.035	1.050	1.044	1.042	1.040
1.362	1.340	1.285	1.268	1.250
1.884	1.735	1.590	1.550	1.520

3.2. Experimental validation

3.2.1. Un-scanned beams

ρ_S and ρ_N of the tested non-water materials were derived from the experiments as shown in table 1. The measured PIDs behind 40% K_2HPO_4, milk, and olive oil are plotted as a function of the distance from R_{90} in figure 3, along with the uncorrected PIDs for helium-, carbon-, oxygen-, and neon-ion beams. The measured PIDs behind water were almost perfectly reproduced by the uncorrected PIDs, and thus they are not shown in the graphs. For 40% K_2HPO_4, the measured PIDs upstream of R_{90} were higher than the uncorrected PIDs. Conversely, for olive oil, the measured PIDs upstream of R_{90} were lower than the uncorrected PIDs. The difference between the measured PIDs behind the materials and the uncorrected PIDs were larger for heavier ions due to their increased nuclear interaction probabilities. Due to high water-equivalence of milk regarding inelastic nuclear interactions, the differences between the measured and uncorrected PIDs were small for all ion beams. In figure 3, we also show the corrected PIDs with ρ_S and ρ_N summarized in table 1. For all non-water materials and projectile ions, the corrected PIDs reasonably reproduced the measured PIDs behind the materials.

The factors ξ_{uc} and ξ_c for the non-water materials in the three regions were derived for the four ion beams, and summarized in table 3 as forms of relative dosimetric errors of $\xi_{uc} - 1$ and $\xi_c - 1$, respectively. The value of

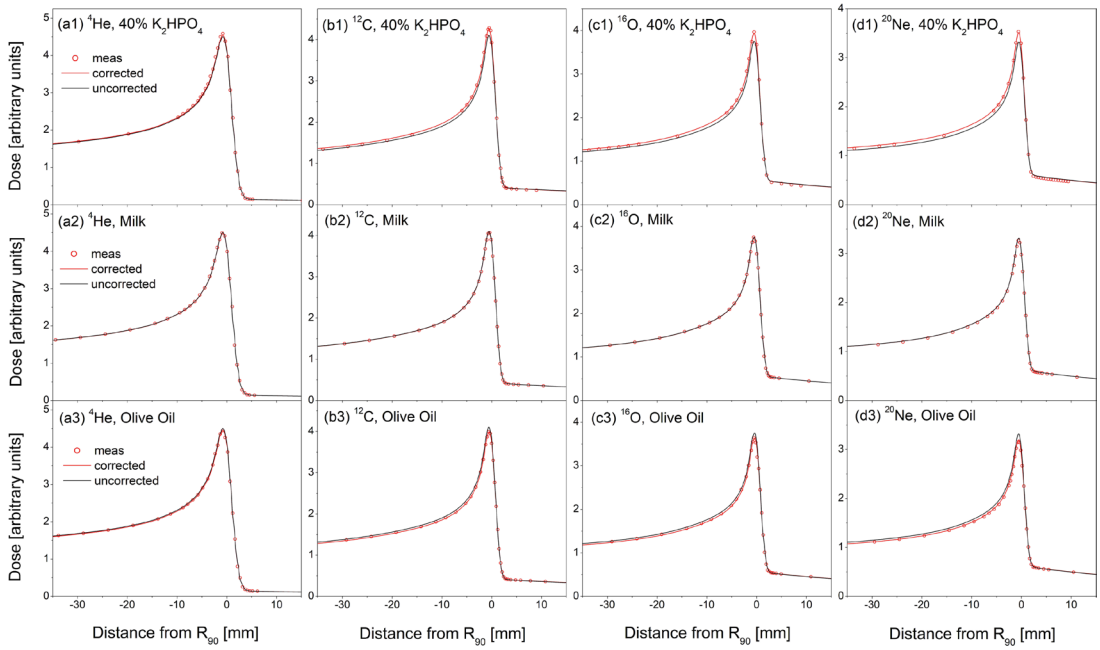

Figure 3. The measured (red open circles), corrected (red solid curve), and uncorrected (black solid curve) PIDs of helium- (1st column), carbon- (2nd column), oxygen- (3rd column), and neon-ion beams (4th column) behind the 100 mm thick layer of 40% K_2HPO_4 (top row), milk (middle row), and olive oil (bottom row).

Table 3. The relative dosimetric errors $\xi_{uc} - 1$ and $\xi_c - 1$ for ethanol, 40% K_2HPO_4, olive oil, and milk in the proximal, peak, and tail regions of helium-, carbon-, oxygen-, and neon-ion beams.

		Proximal		Peak		Tail	
Projectile	Material	$\xi_{uc} - 1$	$\xi_c - 1$	$\xi_{uc} - 1$	$\xi_c - 1$	$\xi_{uc} - 1$	$\xi_c - 1$
^{4}He	Ethanol	0.006	0.010	0.004	0.008	0.007	0.000
	K_2HPO_4	−0.002	−0.008	0.019	0.009	−0.029	−0.017
	Olive oil	−0.003	0.006	−0.008	0.003	0.025	0.016
	Milk	0.000	0.002	0.003	0.004	0.007	0.004
^{12}C	Ethanol	−0.013	0.005	−0.020	0.000	0.020	0.008
	K_2HPO_4	0.015	−0.014	0.042	0.003	−0.051	−0.030
	Olive oil	−0.015	0.008	−0.028	0.001	0.026	0.010
	Milk	−0.001	0.001	−0.002	0.000	0.002	0.001
^{16}O	Ethanol	−0.012	0.006	−0.021	0.001	0.021	0.011
	K_2HPO_4	0.025	−0.012	0.050	0.003	−0. 059	−0.040
	Olive oil	−0.015	0.010	−0.030	0.002	0.030	0.016
	Milk	−0.001	0.001	−0.004	−0.001	−0.001	−0.002
^{20}Ne	Ethanol	−0.017	0.006	−0.026	−0.001	0.017	0.007
	K_2HPO_4	0.030	−0.016	0.059	0.001	−0.074	−0.060
	Olive oil	−0.032	−0.002	−0.043	−0.006	0.013	0.002
	Milk	0.000	0.002	0.003	0.004	0.005	0.004

$\xi_{uc} - 1$ quantifies the water nonequivalence of the material regarding nuclear interactions, while the accuracy of the PID correction method can be evaluated by $\xi_c - 1$.

For milk, $\xi_{uc} - 1$ values in all three regions were almost zero for all ion beams, implying the water equivalence of milk in inelastic nuclear interactions. For ethanol and olive oil, $\xi_{uc} - 1$ values in the proximal and peak regions were less than zero indicating increased attenuation of primary ions in these materials as compared to that in water, while $\xi_{uc} - 1$ values in the tail region were greater than zero with increased production of secondary fragments. The exception was the helium-ion beam in ethanol with $\xi_{uc} - 1$ being greater than zero in all three regions. For 40% K_2HPO_4, coversely, $\xi_{uc} - 1$ values in the proximal and peak regions were greater than zero indicating the reduced attenuation of primary ions in the material as compared to that in water, while those in the tail region were less than zero with reduced production of secondary fragments. The exception was again for the helium-ion beam in the proximal region. The dose difference between the measured and uncorrected PIDs was

greater for heavier ions due to their increased nuclear interaction probabilities. For instance, $\xi_{uc} - 1$ in the peak region of the neon-ion beam behind olive oil and 40% K_2HPO_4 had values of −0.043 and 0.059, respectively, while they were −0.008 and 0.019 for the helium-ion beam.

For all ion beams and materials except for 40% K_2HPO_4, the dosimetric error $|\xi_c - 1|$ was $\leqslant$0.01 in the proximal and peak regions and <0.02 in the tail region. These results verified the accuracy and usefulness of the extended PID correction. For 40% K_2HPO_4, the dosimetric error was also reduced by the extended PID correction. However, the accuracy of the correction was slightly lower as compared to that for other materials.

3.2.2. *Scanned beams*

The measured dose distributions along the central beam axis of four ion beams behind a 100 mm thick layer of olive oil along the central beam axis were compared with the planned dose distributions with the presented PID correction in figure 4. For all ion beams, the planned dose distribution agreed well with the measured distribution in all the regions. The dose calculation errors in the planned distributions averaged over the SOBP were only −0.1%, −0.3%, −0.4%, and −0.2% for helium-, carbon-, oxygen-, and neon-ion beams, respectively. The recalculated dose distributions without the PID correction are also shown in figure 4. For all ion beams, the recalculated distributions overestimated the measured doses in the proximal and SOBP regions. The dose calculation errors in the recalculated distributions averaged over the SOBP were 1.1%, 2.0%, 2.2%, and 2.7% for the beams, respectively.

3.3. Case study

3.3.1. *Prostate case*

Figure 5 compares the planned (corrected) and recalculated (uncorrected) dose distributions of the prostate cancer case. The PTV was well covered by the 95%-isodose line of the planned dose distributions for all ion species. The percentage dose difference map given by $\Delta = (D_{uc} - D_c)/D_{pre} \times 100$ highlighted that the uncorrected dose in the anterior part of the PTV was higher ($\lesssim$0.6%) than the corrected dose. In contrast, the uncorrected dose in the posterior part of the PTV was lower ($\lesssim$0.8%) than the corrected dose for oxygen- and neon-ion beams. The difference between the corrected and uncorrected doses averaged over the PTV was, however, at most 0.4% for all ion beams as shown in the dose volume histograms (DVHs) of the PTV (4th row in figure 5).

3.3.2. *Uterine case*

Figure 6 shows the planned (corrected) and recalculated (uncorrected) dose distributions of the uterine case. For all ion beams, the PTV was well covered by the 95%-isodose line of the planned dose distribution. The uncorrected dose in the PTV was higher than the corrected distribution especially for heavier ion beams, e.g. oxygen- and neon-ion beams. The dose difference reached to 4% at the left part of the PTV for the neon-ion beam.

4. Discussion

The accuracy of the PID correction method for the muscle-substitute material (milk) and adipose-substitute materials (ethanol and olive oil) was high. The relative dosimetric errors $|\xi_c - 1|$ were $\leqslant$ 0.01 for the materials in the proximal and peak regions. The error was < 0.02 even for the tail region. Conversely, the accuracy of the correction method was somewhat lower for 40% K_2HPO_4 especially in the proximal and tail regions. For an unscanned neon-ion beam penetrating a 100 mm thick layer of 40% K_2HPO_4, $|\xi_c - 1|$ values were 0.016 and 0.060 in the proximal and tail regions, respectively. For neon-ion beams penetrating a ~100 mm thick layer of cortical bone, dosimetric errors of the similar order, i.e. 1.6% and 6.0% in the proximal and tail regions, are anticipated in patient dose calculation even with the PID correction method. The presented correction method ignores the unpredictable effect of water nonequivalence of the body tissues on the dose contribution from the heavy fragments (second component). The unsuitability of this approximation for materials with high effective atomic numbers may be one of the reasons for the observed large dosimetric error. A detailed Monte Carlo study of the energy spectrum of fragment particles in various non-water materials would be able to identify the reasons; however, that is beyond the scope of this study. According to the standard tissue data in the ICRP Publication 110 (ICRP 2009), muscle and adipose tissues occupy ~70% of the human body as volume fraction, while bony tissues occupy only ~10%. The high accuracy of the correction method for muscle and adipose tissues is thus more important than that for bony tissues in clinical treatment planning.

As discussed elsewhere (Inaniwa *et al* 2015a, 2015c), the probability of inelastic nuclear interactions per energy loss is approximated as $\rho_N/\rho_S \propto \sum_i w_i Z_i^{-1/3} / \left(Z^{-1/3}\right)_w$ where Z_i and $\left(Z^{-1/3}\right)_w$ are the atomic number of element i and the weighted average of $Z^{-1/3}$ for water, respectively. This simplified description implies that the lower the effective atomic number of the material as compared to water, the more the projectile ions undergo nuclear interactions until they come to rest in the material, and vice versa. Among human body tissues, adipose tissues have lower effective atomic numbers, while bony tissues have higher effective atomic numbers. To

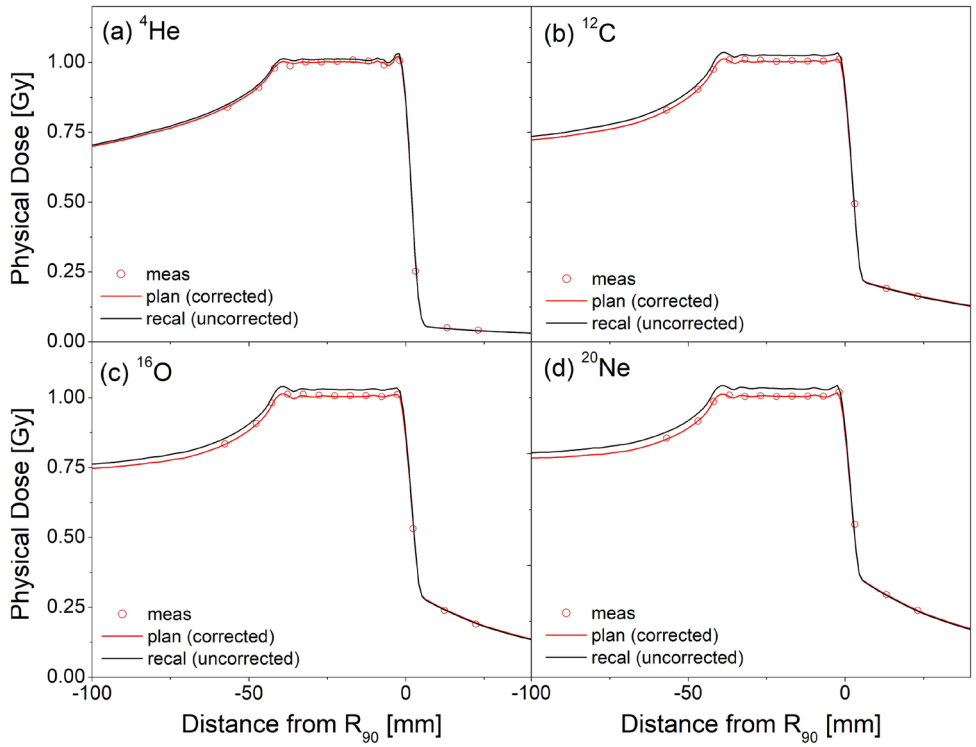

Figure 4. The measured dose distributions of (a) helium-, (b) carbon-, (c) oxygen-, and (d) neon-ion beams along the central beam axis behind a 100 mm thick layer of olive oil (open circles). The red curves are the planned dose distributions with the PID corrections, while the black curves are the recalculated dose distributions without the PID corrections.

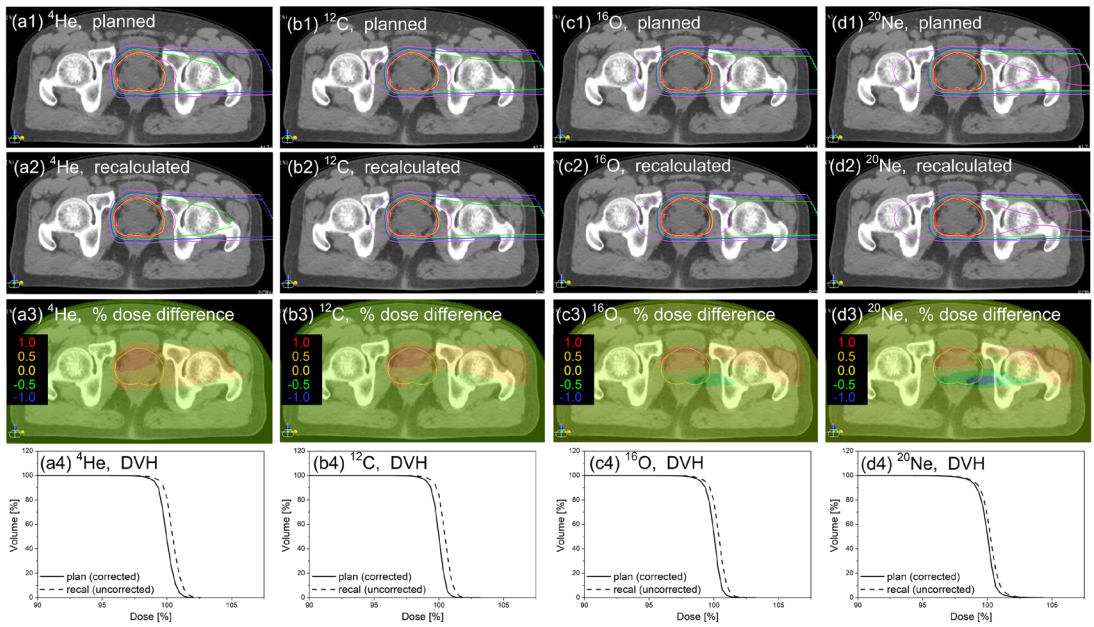

Figure 5. Comparisons of planned (corrected) dose distributions (1st row) and recalculated (uncorrected) dose distributions on a iso-center plane without the PID corrections (2nd row), together with percentage dose difference maps (3rd row) for the prostate case using helium- (1st column), carbon- (2nd column), oxygen- (3rd column), and neon-ion beams (4th column). In all panels, the solid yellow line outlines the planning target volume (PTV). The dose-volume histograms (DVHs; 4th row) of the planned (solid curve) and recalculated dose distributions (dashed curve) in the PTV.

a first order approximation, the geometrical cross section of a projectile nucleus of mass number A with a target nucleus is proportional to $A^{2/3}$ (Sihver *et al* 1993), implying the heavier the projectile ions the more they undergo nuclear interactions, and vice versa. These properties of nuclear interactions provide a qualitative explanation for the observed dose differences in figures 5 and 6. In the prostate case (figure 5), the treatment beam delivered to the anterior part of the PTV and penetrating the subcutaneous and visceral fats underwent more nuclear interac-

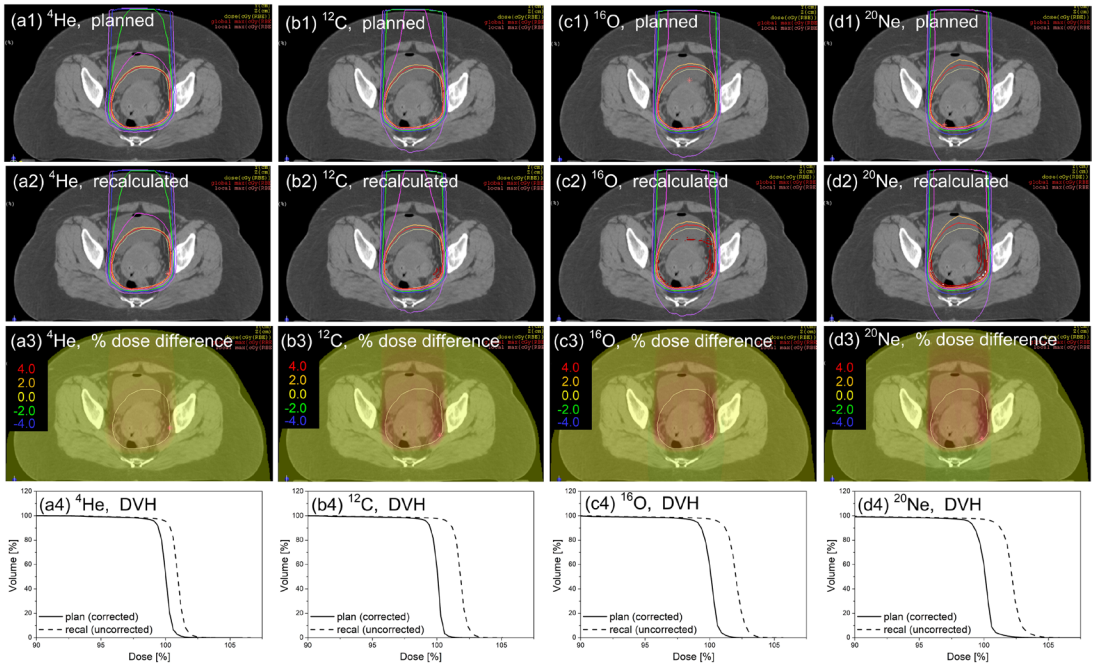

Figure 6. Comparisons of planned (corrected) dose distributions (1st row) and recalculated (uncorrected) dose distributions on a iso-center plane without the PID corrections (2nd row), together with percentage dose difference maps (3rd row) for the uterine case using helium- (1st column), carbon- (2nd column), oxygen- (3rd column), and neon-ion beams (4th column). In all panels, the solid yellow line outlines the planning target volume (PTV). The DVHs (4th row) of the planned (solid curve) and recalculated dose distributions (dashed curve) in the PTV.

tions as compared to the case in water. In contrast, the treatment beam delivered to the posterior part of the PTV and penetrating the femur underwent fewer nuclear interactions as compared to the case in water, which was pronounced for heavier ions, e.g. oxygen and neon ions. However, the percentage dose difference Δ between the corrected and uncorrected doses within the PTV was -0.8% at maximum for all ion beams. In the uterine case (figure 6), the whole treatment beam penetrated approximately 7 cm of subcutaneous fat, and part of it additionally penetrated approximately 10 cm of visceral fat. Consequently, more projectile ions underwent nuclear interactions until they come to rest as compared to the case in water. The dose difference between the corrected and uncorrected doses was pronounced for the heavier ions. For the neon-ion beam, we observed Δ of 2.2% within target in average and 3.9% at maximum.

The computation time required for dose calculations with the nuclear interaction correction was almost the same as that required for the calculations without correction, within 5%. Therefore, the nuclear interaction correction should be routinely used in patient dose calculations of helium-, carbon-, oxygen-, and neon-ion beams.

5. Conclusion

Dose calculations of charged-particle therapy based on the PID measured in water with patient heterogeneity correction by path length scaling for the beam range may cause dose calculation errors due to water nonequivalence of body tissues in nuclear interactions. Previously, we had developed the PID correction method for scanned carbon-ion beams to account for the dosimetric errors in patients. In this study, we extended the PID correction method to patient dose calculations of helium-, oxygen-, and neon-ion beams. The dose calculation errors due to water-nonequivalence of non-water materials were reasonably reduced by the correction method for all ion species. In un-scanned beams penetrating a 100 mm thick layer of olive oil, the dose calculation errors around the Bragg peak of -0.8%, -2.8%, -3.0%, and -4.3% for helium-, carbon-, oxygen-, and neon-ion beams, respectively, were reduced to 0.3%, 0.1%, 0.2%, and -0.6% by the correction method. Similarly, in un-scanned beams penetrating a 100 mm thick layer of 40% K_2HPO_4, the dose calculation errors around the Bragg peak of 1.9%, 4.2%, 5.0%, and 5.9% were reduced to 0.9%, 0.3%, 0.3%, and 0.1% by the correction method. The availability of the PID correction method in treatment planning was verified by the scanned ion beams penetrating a 100 mm thick layer of olive oil. The dose calculation errors of the uncorrected distribution averaged over the SOBP were 1.1%, 2.0%, 2.2%, and 2.7%, while they were reduced to -0.1%, -0.3%, -0.4%, and -0.2% by the correction method. A treatment planning study was performed for two clinical cases to investigate the influence of water nonequivalence of body tissues on tumor dose. The influence can be substantial for some extreme cases especially for heavier ions, e.g. oxygen or neon ions. The presented method can reduce

these potential dosimetric errors in clinical treatment planning. The correction method offers the accuracy and simplicity required in treatment planning of helium-, carbon-, oxygen-, and neon-ion radiotherapy.

Acknowledgments

This work was partially supported by a Grant-in Aid for Scientific Research (No. 17K09074) from the Japan Society for Promotion of Science (JSPS).

ORCID iDs

Nobuyuki Kanematsu https://orcid.org/0000-0002-2534-9933

References

Agostinelli S *et al* 2003 Geant4—a simulation toolkit *Nucl. Instrum. Methods. Phys. Res.* A **506** 250–303
Blakely E A, Tobias C A, Yang T C H, Smith K C and Lyman J T 1979 Inactivation of human kidney cells by high-energy monoenergetic heavy-ion beams *Radiat. Res.* **80** 122–60
Böhlen T T, Bauer J, Dosanjh M, Ferrari A, Haberer T, Parodi K, Patera V and Mairani A 2013 A Monte Carlo-based treatment-planning tool for ion beam therapy *J. Radiat. Res.* **54** i77–i81
Böhlen T T, Brons S, Dosanjh M, Ferrari A, Fossati P, Heberer T, Patera V and Mairani A 2012 Investigating the robustness of ion beam therapy treatment plans to uncertainties in biological treatment parameters *Phys. Med. Biol.* **57** 7983–8004
Gottschalk B 2010 On the scattering power of radiotherapy protons *Med. Phys.* **37** 352–67
ICRP 2009 *Adult Reference Computational Phantoms (Publication 110)* (Ottawa: International Commission on Radiological Protection)
ICRU 1992 *Photon, Electron, Proton and Neutron Irradiation Data for Body Tissues (Report 46)* (Bethesda, MD: International Commission on Radiation Units and Measurements)
Inaniwa T and Kanematsu N 2015 A trichrome beam model for biological dose calculation in scanned carbon-ion radiotherapy treatment planning *Phys. Med. Biol.* **60** 437–51
Inaniwa T and Kanematsu N 2016 Effective particle energies for stopping power calculation in radiotherapy treatment planning with protons and helium, carbon and oxygen ions *Phys. Med. Biol.* **61** N542–50
Inaniwa T and Kanematsu N 2018 Adaptation of stochastic microdosimetric kinetic model for charged-particle therapy treatment planning *Phys. Med. Biol.* **63** 095011
Inaniwa T, Kanematsu N, Hara Y and Furukawa T 2015a Nuclear-interaction correction of integrated depth dose in carbon-ion radiotherapy treatment planning *Phys. Med. Biol.* **60** 421–35
Inaniwa T, Kanematsu N, Hara Y, Furukawa T, Fukahori M, Nakao M and Shirai T 2014 Implementation of a triple Gaussian beam model with subdivision and redefinition against density heterogeneities in treatment planning for scanned carbon-ion radiotherapy *Phys. Med. Biol.* **59** 5361–86
Inaniwa T, Kanematsu N, Matsufuji N, Kanai T, Shirai T, Noda K, Tsuji H, Kamada T and Tsujii H 2015b Reformulation of a clinical-dose system for carbon-ion radiotherapy treatment planning at the National Institute of Radiological Sciences, Japan *Phys. Med. Biol.* **60** 3271–86
Inaniwa T, Kanematsu N, Noda K and Kamada T 2017 Treatment planning of intensity modulated composite particle therapy with dose and linear energy transfer optimization *Phys. Med. Biol.* **62** 5180–97
Inaniwa T, Kanematsu N, Sato S and Kohno R 2016 A dose calculation algorithm with correction for proton-nucleus interactions in non-water materials for proton radiotherapy treatment planning *Phys. Med. Biol.* **61** 67–89
Inaniwa T, Kanematsu N, Tsuji H and Kamada T 2015c Evaluation of hybrid depth scanning for carbon-ion radiotherapy *Med. Phys.* **39** 2820–5
Kanematsu N, Inaniwa T and Koba Y 2012 Relationship between electron density and effective densities of body tissues for stopping, scattering, and nuclear interactions of proton and ion beams *Med. Phys.* **39** 1016–20
Kanematsu N, Inaniwa T and Nakao M 2016 Modeling of body tissues for Monte Carlo simulation of radiotherapy treatments planned with conventional x-ray CT systems *Phys. Med. Biol.* **61** 5037–50
Kanematsu N, Matsufuji N, Kohno R, Minohara S and Kanai T 2003 A CT calibration method based on the polybinary tissue model for radiotherapy treatment planning *Phys. Med. Biol.* **48** 1053–64
Kopp B, Mein S, Dokic I, Harrabi S, Böhlen T T, Heberer T, Debus J, Abdollahi A and Mairani A 2020 Development and validation of single field multi-ion particle therapy treatments *Int. J. Radiat. Oncol. Biol. Phys.* **106** 194–205
Krämer M, Scifoni E, Schmitz F, Sokol O and Durante M 2014 Overview of recent advances in treatment planning for ion beam radiotherapy *Eur. Phys. J.* D **68** 306
Krämer M *et al* 2016 Helium ions for radiotherapy? Physical and biological verifications of a novel treatment modality *Med. Phys.* **43** 1995–2004
Kurz C, Mairani A and Parodi K 2012 First experimental-based characterization of oxygen ion beam depth dose distributions at the Heidelberg Ion-Beam Therapy Center *Phys. Med. Biol.* **57** 5017–34
Palmans H and Verhaegen F 2005 Assigning nonelastic nuclear interaction cross sections to Hounsfield units for Monte Carlo treatment planning of proton beams *Phys. Med. Biol.* **50** 991–1000
Schneider U, Pedroni E and Lomax A 1996 The calibration of CT Hounsfield units for radiotherapy treatment planning *Phys. Med. Biol.* **41** 111–23
Schneider U, Pemler P, Besserer J, Dellert M, Moosburger M, Boer J, Pedroni E and Boehringer T 2002 The water equivalence of solid materials used for dosimetry with small proton beams *Med. Phys.* **29** 2946–51
Sihver L and Mancusi D 2009 Present status and validation of HIBRAC *Radiat. Mes.* **44** 38–46
Sihver L, Tsao C H, Silberberg R, Kanai T and Barghouty A F 1993 Total reaction and partial cross section calculations in proton-nucleus ($Z_t \leqslant 26$) and nucleus-nucleus reactions (Z_p and $Z_t \leqslant 26$) *Phys. Rev.* C **47** 1225–36

Sokol O *et al* 2017 Oxygen beams for therapy: advanced biological treatment planning and experimental verification *Phys. Med. Biol.* **62** 7798–813

Tessonnier T, Böhlen T T, Ceruti F, Ferrari A, Sala P, Brons S, Haberrer T, Debud J, Parodi K and Mairani A 2017b Dosimetric verification in water of a Monte Carlo treatment planning tool for proton, helium, carbon and oxygen ion beams at the Heidelberg Ion Beam Therapy Center *Phys. Med. Biol.* **62** 6579–94

Tessonnier T, Mairani A, Brons S, Haberrer T, Debud J and Parodi K 2017a Experimental dosimetric comparison of 1H, 4He, 12C and 16O scanned ion beams *Phys. Med. Biol.* **62** 3958–82

Tobias C A *et al* 1971 Radiological physics characteristics of the extracted heavy ion beams of the bevatron *Science* **174** 1131–4